Oral presentation | Industrial applications
Industrial applications-I
Mon. Jul 15, 2024 4:30 PM - 6:30 PM Room B

[3-B-01] CFD-Based Heat Transfer and Flow Field Investigations of a Heat Recovery Steam Generator for Aero Engine Applications

*Mahmoud El-Soueidan[1], Jannik Häßy[1], Marc Schmelcher[1], Alexander Görtz[1] (1. German Aerospace Center (DLR), Cologne, Germany)

Keywords: Computational Fluid Dynamics, Turbulence Modeling, Heat Recovery Steam Generator

CFD-Based Heat Transfer and Flow Field Investigations of a Heat Recovery Steam Generator for Aero Engine Applications

M. El-Soueidan*, J. Häßy*, M. Schmelcher*and A. Görtz*
Corresponding author: mahmoud.el-soueidan@dlr.de
* German Aerospace Center (DLR), Cologne, Germany

1 Introduction

In aviation, tackling climate-relevant emissions is the main driver for current and future research programs. Researchers in collaboration with aviation industry are putting together a significant amount of effort into reducing environmental impact of the aircraft engine. It is found that non-carbon dioxide emissions, e.g. NO_x and contrails cause the main impact on environmental air pollution when it comes to aviation [1]. The Water-Enhanced Turbofan (WET) presented by MTU Aero Engines is a promising revolutionary propulsion concept to tackle non-carbon dioxide emissions [1, 2].

The WET concept implements a dual fluid thermodynamic cycle similar to the Cheng Cycle to increase thermodynamic cycle efficiency and increase specific power of the engine. Fig. 1 displays a possible architecture of the WET concept presented by Schmitz et al. [2]. In this concept, superheated steam is injected into the core flow of the engine, so that the components downstream of the combustion chamber face an exhaust flow rich in water vapor. The superheated steam is generated by transferring exhaust heat to the cold fluid side in order to preheat, evaporate and superheat liquid water. This heat transfer takes place in a heat recovery steam generator (HRSG) downstream of the low-pressure turbine. Downstream of the HRSG component, a water condensation and recovery unit is integrated into the engine. This unit comprises of a second heat exchanger, named condenser, and a water recovery unit. The condenser cools down the steam loaded exhaust flow below its dewpoint temperature leading to the formation of liquid water droplets in the exhaust flow. The condensed liquid water is then recovered for the closed-loop water cycle of the WET concept in the water recovery unit. The recovered liquid water is compressed to a required level of total pressure and then fed back into the HRSG component again. For more information regarding the WET concept refer to Schmitz et al. [2].
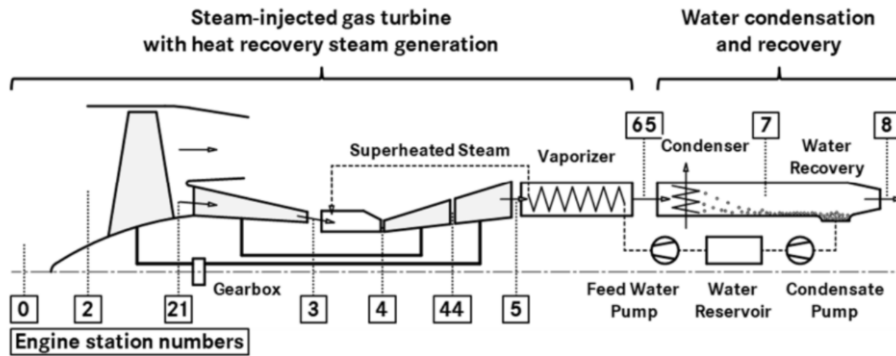
Figure 1: A proposed architecture of the WET concept by [1, 2]

The HRSG poses a novel component for aircraft engine industry as heat exchanger with phase change phenomena on one fluid side have not been integrated into the core flow of aero engines yet. Based on a literature review, there is no publication dealing with the detailed flow field of a HRSG taking into account the setup and boundary conditions of this component in the WET concept.

1

The goal of this publication is, therefore, to present the local and global flow field behaviour of the exhaust flow through a tube bundle arrangement of a possible HRSG setup. Flow characteristics of the flow field, the development of heat transfer coefficient, Nusselt number and the pressure loss along the passages is presented.

2   State of the Art

Regarding the design of the HRSG, there are present studies on different fidelity levels of such a novel component. Thermodynamic cycle computations by Görtz et al. [3] and Ziegler et al. [4] evaluate the WET concept on global scale regarding cycle efficiency and fuel consumption. Preliminary design studies by Schmelcher et al. [5] present a cell based P-NTU method on low-fidelity level to predict the thermodynamic performance of the HRSG on both fluid sides. High fidelity CFD modeling of the HRSG component is necessary to minimize uncertainties in the correlation-based prediction of the heat exchanger. Based on a literature review, there are several publicaitons dealing with the CFD modeling of heat exchanger in aviation.

2.1   CFD Modeling of Heat Exchanger

The heat exchanger modeled for aircraft engine integration often comprise of staggered tube bundle arrangements. Based on a literature review, there are a number of publications dealing with the flow field analysis of tube bundle heat exchanger. Most of the applications for the modeling of tube bundle heat exchanger are ground-based applications. The publications can be divided into numerical analyses conducted to evaluate the heat exchanger performance and experimental work done on validating numerical predictions.

There are several methods available on different fidelity levels to predict the thermdoynamic behaviour of a heat exchanger. Performance cycle computations use simple models to determine the inlet and outlet thermodynamic conditions of the respective component. On component level, there are higher order tools to model the heat exchanger. These tools are based on correlations available in literature for the heat transfer and pressure drop of the respective tube bundle setup. At the DLR Institute of Propulsion Technology, a preliminary design tool is developed to predict the thermodynamic performance of heat exchanger setups for aero engine applications named PreHEAT. For detailed information on the setup and workflow of the tool refer to Schmelcher et al. [5].

There are several publications dealing with the design and analysis of heat exchanger setups integrated into aero engine applications. The most dominant example, is a developed heat exchanger setup for the Intercooled and Recuperated Aero Engine (IRA). The exhaust gas recuperator of the IRA engine cools down dry exhaust gas and heats up compressor exit air to reduce fuel burn and inrease efficiency of the engine. A group of researchers at the University of Thessaloniki published detailed work on the numerical analysis of a possible setup of the recuperator for the IRA engine, see Missirlis et al. [6, 7, 8, 9], Yakinthos et al. [10] and Vlahostergios et al. [11]. The publications are divided into four major parts regarding the CFD analysis: 2D CFD simulation of a representative domain of the heat exchanger, the derivation of a porosity model for the heat exchanger, the validation of the derived porosity model and the analysis and optimization of the heat exhaust duct of the IRA engine together with the integrated exhaust recuperator.

Missirlis et al. [8] use 2D CFD modeling approach to analyze the local and global flow field of a possible tube bundle setup of the exhaust gas recuperator. The 2D CFD domain models a characteristic flow path of the exhaust gas. The Reynolds-Averaged-Navier-Stokes (RANS) equations are used to model the flow field behaviour, so that conservation of mass, momentum and energy is fulfilled. There is not a transient modeling of the flow field as preliminary studies show that the average CFD results of the flow field are not influenced by the unstaediness of the flow. The turbulence is modeled using the shear-stress turbulence model developed by Menter. The fluid inlet into the domain is modeled as a velocity inlet together with a static pressure outlet. The cold fluid side is considered by defining tube wall temperatures. The results of the analysis showed that the local cross flow of elliptic tubes can be divided into an X-type main flow, a wake region and an acceleration region.

2.2 The HRSG of the WET Concept

The HRSG of the WET concept is located in the exhaust flow downstream of the turbine section. The existing enthalpy potential of the exhaust flow is used to transfer heat from the exhaust side to the cold fluid side of the HRSG. The cold fluid of the evaporator is liquid water on a required pressure level being evaporated heat transfer taking place. The superheated steam has to meet a certain temperature and pressure level in order to be injected into the core flow of the engine after feeding a steam turbine to drive a third shaft for the compressor section of the WET concept. The pressure level of the superheated steam downstream of the steam turbine (before the injection into the core flow of the engine) still has to be higher than the core pressure at location of the injection. Thus, the integration of such a novel component into the aero engine and the engine operating condition are the main driver for the required inlet and outlet states of the HRSG component.

The amount of heat transferred from the hot fluid side to the cold fluid side of the evaporator depends on the driving temperature difference between both fluid sides and the overall thermal resistance of both fluid sides. As the heat transfer coefficient of the steam loaded exhaust gas is at least one order of magnitude lower than the heat transfer coefficients on the water side, the main thermal resistance determining the heat transfer rate for a given temperature delta is the thermal resistance of the exhaust side. Thus, the maximization of the exhaust side heat transfer coefficient and therefore the reduction of the exhaust sides's thermal resistance is one major challenge when designing the HRSG for the WET concept. The fluid flow through the HRSG on the exhaust side induces pressure loss to the flow. The pressure loss on the exhaust side of the evaporator transfers directly into a propulsive efficiency loss of a turbofan engine. Therefore, it is important that the design of the HRSG considers not only the thermal, but also the hydraulic behaviour of both fluid sides minimizing the pressure losses on the exhaust side.

The setup of the HRSG is modeled by a tube bundle arrangement. Fig. 2 shows a possible arrangement of tubes for the HRSG. A defined number of parallel tubes are placed next to each other forming a staggered arrangement of the tubes. Each tube consists of a defined number of bendings defining the vertical dimension of the HRSG. The tube sections between each bending of the tube are named flow passages, see Fig. 2 left. The current setup consists of a total number of 25 flow passages and a defined number of parallel tubes. Normal to flow direction $s_1/d = 1.463$ determines the transversal distance between the tubes and $s_2/d = 1.146$ determines the distance of the tubes in flow direction of the exhaust flow. Inside the parallel tubes, liquid water is present and outside of the tube there is crossflow of steam loaded exhaust flow, so that the HRSG is modeled with a cross counter flow configuration. On global scale, the flow direction of the exhaust flow points into the opposite flow direction of the water side. On local scale however, the flow vectors of exhaust side and water side are normal to each other.
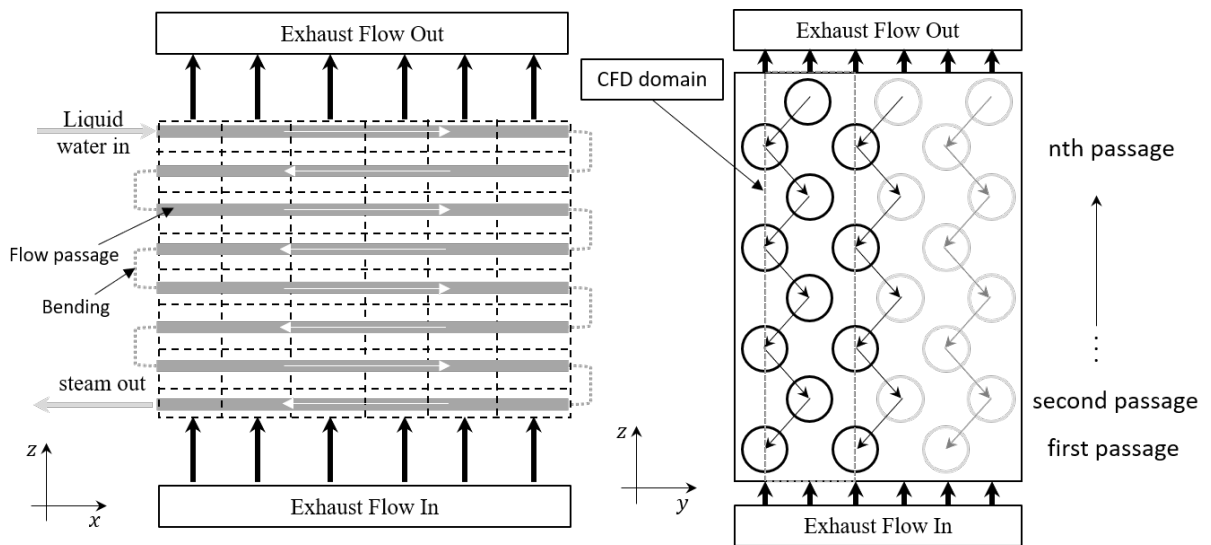
Figure 2: Heat Exchanger setup: Global view (left) and cross-sectional view (right)

2.3 CFD Analysis of the HRSG

CFD analysis of the HRSG is necessary as correlation-based predictions with preliminary design tools are accompanied by uncertainties. In order to minimize these uncertainties, CFD models have to be developed. Considering computational costs, it is not possible to model the HRSG with a full scale 1:1 3D CFD model. Therefore, only 2D steady RANS simulations are performed to predict the thermal and hydraulic behaviour of the HRSG using the commercial solver *Ansys Fluent*. A possible setup of the CFD domain is presented in Fig. 2. There are tubes located in the center as well as on the left and right hand side of the CFD domain. As the domain is later oriented horizontally for the CFD simulation, there will be top and bottom tubes and center tubes. As state of the art CFD software are not capable of modeling phase change phenomena yet, only the exhaust side of the HRSG is modeled with CFD. The water side in the CFD model is considered by defining tube wall temperatures for the respective CFD contours. This leads also to the requirement of conjugated heat transfer computations by PreHEAT computing the tube wall temperatures and integrating the exhaust side CFD results into the its analysis.

In [12] a method is presented to couple conjugated heat transfer computations by PreHEAT with high fidelity CFD computations. The presented methodology is applied in this publication for the generation of the presented CFD results. A specific x-coordinate location of the cells in PreHEAT has to be selected as the *coupling plane* for the coupled analysis between PreHEAT and CFD. The implemented coupled analysis feeds back key coupling paramters between PreHEAT and CFD, see Fig. 2. The key coupling parameters of the closed-loop analysis between PreHEAT and CFD are tube wall temperatures and correction values for the exhaust side heat transfer coefficients and pressure losses. Either absolute *delta* values for the correction values or dimensionless ratios, referred to as *factors*, can be used for the feedback of heat transfer coefficient and pressure loss. For the convergence of the coupled analysis, a suitable reference temperature based on an *energy balance approach* for the computation of the exhaust side CFD-based heat transfer coefficient has to be set for the coupled analysis. Several criteria are defined to ensure convergence of global heat transfer and pressure loss between PreHEAT and CFD analysis.

Applying the presented settings and boundary conditions for the coupled analysis between PreHEAT and CFD results in a total number of four coupling iterations to meet the defined convergence criteria in El-Soueidan et al. [12]. The error between the transferred heat between PreHEAT and CFD is reduced to values below 1% leading to an error in outlet temperature of below 0.1%. The absolute pressure loss over the domain also converges with an error of below 0.1% between PreHEAT and CFD. The maximum relative change in tube wall temperatures is reduced by four orders of magnitude. Therefore, not only the global performance parameter are converged, but it is also ensured that there is no relevant change in the inputs for the CFD computation considering the convergence of tube wall temperatures. For more details on the convergence behaviour of the coupled analysis refer to [12].

For the same heat exchanger setup, in [12] a total number of five meshes are investigated to identify a suitable mesh for the CFD computations within a coupled analysis between PreHEAT and CFD. The meshes for CFD analysis are designed, so that close to the wall the dimensionless wall distance falls below $y^+ < 1$. It is shown that the computed results of the CFD analysis depend on the applied numerical mesh for the CFD computation. At the same time, the numerical effort of a CFD computation with a higher number mesh elements increases exponentially with increased number of elements. Therefore, a mesh with nearly 900.000 elements is selected to strike a balance between computational effort of the CFD computation and the accuracy of the CFD results. For more information on the mesh details refer to [12].

Inside the tube bundle arrangement, the fluid state normal to flow direction for each flow passage is monitored by placing rakes at the respective position. The rake's x-position downstream the last tube row (*outlet rake*) and the rake position for the rake upstream the first tube row (*inlet rake*) is computed based on a dimensionless distance:

$$x_{rake,in} = x_{m,first} - \frac{1}{2}d - \left(\frac{f}{d}\right)_{in} \cdot d. \tag{1}$$

$$x_{rake,out} = x_{m,last} + \frac{1}{2}d + \left(\frac{f}{d}\right)_{out} \cdot d. \tag{2}$$

4

3   Methodology

The presented results of the coupled analysis are based on the settings of the coupled approach as stated in the previous section. The *center* x-coordinate of the heat exchanger setup in PreHEAT is chosen as the coupling plane between CFD and PreHEAT. The *delta* correction methods for the correction of exhaust side heat transfer coefficient and pressure losses is applied. The convergence criteria are set according to the suggestions made in [12]. The *energy balance based reference temperature* is chosen as reference for the computation of the heat transfer coefficient and thus for the Nusselt number.

As the unsteadiness of the flow field does not influence the average CFD results [8], the flow field is modeled to be steady. Due to its numerical stability, the $k\omega$-SST turbulence model is used for turbulence modeling in the domain. The inlet boundary is modeled as velocity inlet whereas the outlet boundary is modeled as pressure outlet. Top and bottom boundary are set to be modeled as periodic boundaries. The tube walls are modeled with a no slip wall condition and a tube wall temperature computed by PreHEAT. The boundary conoditions for the presented setup are listed in Tab. 1. The turbulence boundary conditions are defined by setting a turbulent length scale as a half of the tube diameter and a turbulence intensity based on generic assumptions as no experimental data are available. The CFD simulation is considered as converged if the change in mass flow imbalance and pressure loss fall below four orders of magnitude and the enthalpy change falls below seven orders of magnitude.

Table 1: Boundary Conditions for the CFD computations

Parameter	Boundary	Value	Unit
Velocity	inlet	8.27	m/s
Total temperature	inlet	816.5	K
Turbulence intensity level	inlet	5	%

The exhaust flow of the WET concept entering the HRSG on the exhaust side is formed by the turbine exhaust flow containing high amounts of water vapor. The fluid properties of the steam loaded exhaust flow are computed by using user-defined functions in *Ansys Fluent*. The approach describes an ideal gas composed by ideal gases whereas the modeling approach is presented in El-Soueidan et al. [13]. The required gas model settings for the gas model in the CFD simulation are set according to the settings proposed in [12].

PreHEAT applies correlations presented in VDI heat atlas [14] for the heat transfer and pressure loss on the exhaust side. The heat transfer on the water side is computed also based on VDI heat atlas correlations for both, heat transfer and pressure loss except for the two-phase region. Here, the Friedel correlation as presented in Thome et al. [15] is used for the computation of the pressure losses of the water side and the correlation by Borishanksij as presented in Thome [15] is used for the computation of the water side heat transfer coefficients in the two-phase region.

The flow field and heat transfer investigations are presented by computing several similarity parameters like Reynolds number, Nusselt number and the heat transfer coefficient. Each of the mentioned parameters are bound to specific definitions of a reference length, a reference velocity or a reference temperature. These used reference values depend on the applied correlation for heat transfer and pressure loss. Therefore, the definition of this parameters presented in the present publication is outlined.

Since the flow velocity varies along its path through the CFD domain, a reference velocity is chosen to define the Reynolds number. The velocity at the minimum cross-sectional u_{Amin} area is used as reference for the computation of the Reynolds number. The tube diameter is considered as reference length for the Reynolds Number. Finally, the Reynolds number is computed to [14]:

$$\text{Re}_{\text{D}} = \frac{u_{\text{Amin}} \cdot \frac{\pi}{2}d}{\nu} \tag{3}$$

The parameter ν denotes the kinematic viscosity being computed on the reference temperature for the current flow passage and d is the tube's outer diameter being constant for the whole tube bundle arrangement.

The CFD-based exhaust side heat transfer coefficient α_{CFD} is calculated based on the CFD-based computed local wall heat flux distribution . An area weighted average of the local wall heat flux distribution $\dot{q}$ is used to compute the area weighted average of the respective tubes's heat transfer coefficient to, see Eq. (4).

$$\alpha_{\text{CFD}} = \frac{\dot{q}}{T_{\text{w}} - T_{\text{ref}}} \tag{4}$$

The parameter T_{ref} denotes the reference temperature of the current flow passage used for the computation of the heat transfer coefficient. In [12] several approaches for chosing the reference temperature are presented. T_w represents the tube wall temperature being an input computed by the preliminary design tool PreHEAT. The correlation-based exhaust side heat transfer coefficient is computed based on a computed Reynolds number and the given Nu-Re correlation for the heat transfer on the exhaust side.

The Nusselt number Nu_D of one CFD contour in this publication is computed based on the diameter as reference length to:

$$\text{Nu}_{\text{D}} = \frac{\alpha \cdot \frac{\pi}{2} d}{\lambda} \tag{5}$$

The parameter λ represents the thermal conductivity of the exhaust flow evaluated at the respective reference temperature for the heat transfer coefficient.

4   Results

In this chapter, the results of the current publication are presented. There are a total number of six subsections starting with *4.1 Global Performance of the HRSG* followed by *4.2 Flow Field Analysis*, *4.3 The Local Heat Transfer Coefficient*, *4.4 Thermal Analysis*, *4.5 Hydraulic Analysis* and *4.6 Rake Position Dependency*.

4.1   Global Performance of the HRSG

The HRSG transfers heat from the exhaust side of the evaporator to the water side cooling down the exhaust flow and using the transferred heat in order to generate superheated steam. A novelty in this heat exchanger for aircraft engines is the phase change taking place on the cold fluid side. This effects the tubes' wall temperatures among the passages in comparison to single-phase heat exchanger designed for other aircraft engine concepts. The reduction of the exhaust flow temperature and the resulting tube wall temperature along the passages can be seen in Fig. 3. Due to the cross-counterflow configuration of
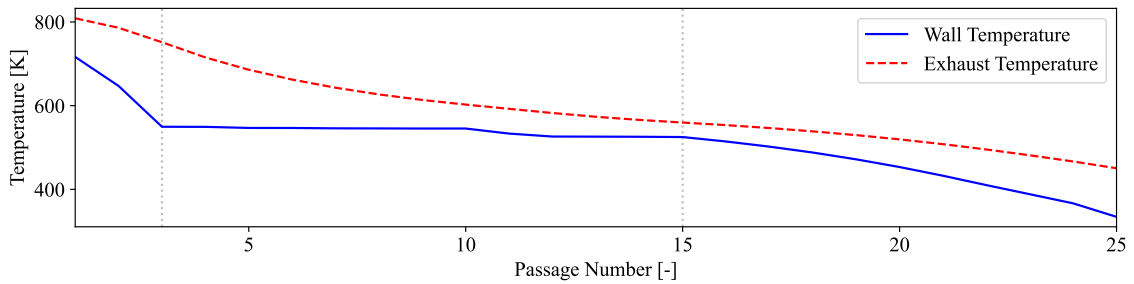
Figure 3: Temperature profile of the wall temperature and the exhaust flow along the flow passages

the heat exchanger, the exhaust flow entering the tube bundle arrangement sees high tube wall temperatures in the first flow passages and low tube wall temperatures in the last flow passages. The vertical lines present the change of flow regime on the water side. Upstream of passage three, on the water side superheating of the generated vapor takes place. Downstream of passage three and upstream of passage 15, the evaporation process takes place recognizable due to the constant tube wall temperature in this region. For the presented setup, the minimal temperature difference between exhaust flow and water side occurs at the entry into the evaporation region. Downstream of passage 15, the liquid water entering the HRSG is therefore preheated increasing the temperature difference between both fluid sides.
Within the evaporation region of the tube wall temperature profile, a temperature step is recognizable.

This is due to the fact of considering the effect of dryout in the preliminary design computation. Dryout describes the effect that during evaporation, the inner side of the tube wall is not longer fully in touch with liquid water but with steam leading to a decrease of the water side heat transfer coefficient. The decreasing heat transfer coefficient on the water side increases thermal resistance on the water side and therefore the tube wall temperatures. The effect of dryout in the tube walls is considered to take place after the volumetric steam fraction reaches values above 80%.

The overall thermal resistance of both fluid sides and the tube wall together with the driving temperature difference between both fluid sides determines the total amount of transferred heat. In this case, the heat exchanger transfers heat leading to a cool down of the exhaust flow of about $\Delta T_t \approx 375$ K. The generated steam due to the heat transfer process exits the HRSG with a temperature over 700 K whereas a large amount of heat is needed to realize the phase change from liquid fluid state to a single phase steam on the water side. The tubes on the inside are therefore covered with wet steam over a wide range of flow passages.

Due to the cross flow of the tubes in the domain a global exhaust side pressure loss of about $\Delta p_t/p_{tIn} \approx$ 1.17% is induced. The pressure loss on the water are caused by wall friction and the phase change taking place inside the tubes. The global water side pressure loss reaches values of 3.3%. The pressure loss on the exhaust side is expensive in terms of efficiency loss of the aero engine. As previously stated, a loss in total pressure on the exhaust side transfers directly into a loss in propulsive efficiency of the engine. The pressure loss on the water side is less critical as the pressurization of liquid water by a pump at the inlet of the HSRG is very cheap. Therefore, a high safety margin for the required pressure level of water can be applied considering the required pressure level at the exit of the HRSG.

4.2 Flow Field Analysis

The flow field analysis is presented in two steps. First of all, a global view on the contours of velocity, temperature and pressure is given and secondly, local parameter distributions within the flow field are presented to characterize the local flow field behaviour.

4.2.1 Global Flow Field Analysis

Fig. 4a, 4b and 4c present the global velocity, temperature and pressure field of the results of the modeled tube bundle arrangement. The presented contour fields on global scale represent the expected behavior of the fluid flow in the CFD domain. Due to the transferred heat from the exhaust gas into the wall, a cool down of the exhaust flow is recognizable. In combination with mass conservation in the CFD domain, the velocity magnitude of the flow decreases along its path through the tube bundle. It is recognizable

(a) Velocity Magnitude

(b) Static Temperature Field

(c) Static Pressure Field
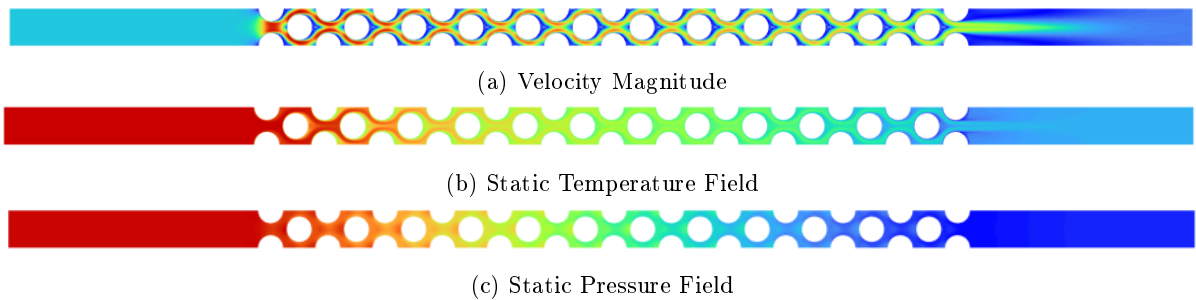
Figure 4: Velocity, Temperature and Pressure Field of the modeled tube bundle setup

that a significant amount of outflow length is important for the flow development downstream of the last tube row. A length of approximately ten times of the diameter of the tubes has been set for the outflow length downstream the last tube row which seems to be a suitable length for outflow development of a steady RANS simulation. The local flow field of the exhaust gas in the tube bundle comprises of an X-type main flow, a recirculation region and an acceleration region. This type of flow behaviour for staggered tube bundle arrangements has been also observed by Umeda and Young [16] and Missirlis et al. [8]. After exiting the tube bundle, a high velocity jet is formed confined by the enlarged recirculation

7

regions of the last top and bottom tubes. Fig 5 shows the mentioned flow regions of the tube bundle by zooming into one tube inside the tube bundle. On the left hand side, the wake region of a center tube is visible. For the present inflow conditions of the flow, the wake region of the tubes is characterized by two
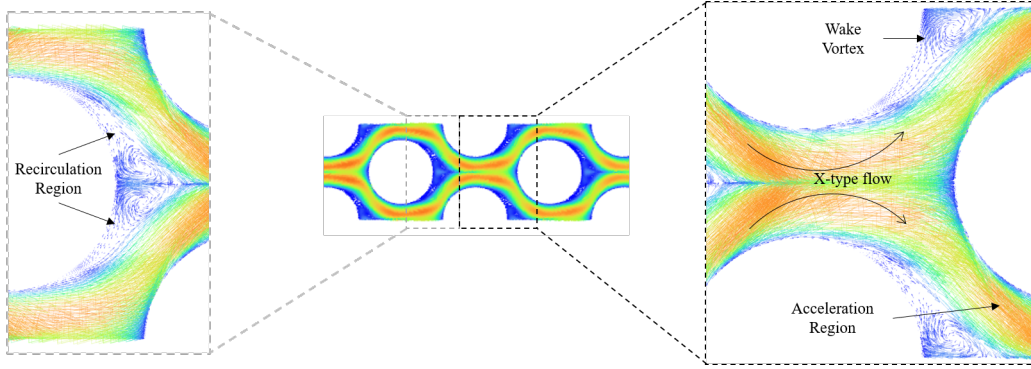
Figure 5: Vector plot of the recirculation region of a tube inside the tube bundle arrangement

counter oriented vortices with a constant level of velocity compared to the main flow. The presence of the vortices forms a virtual contour for the main flow changing the available cross sectional area for the main flow along its path around the tubes and therefore influencing local velocity and pressure levels. The wake regions of the top and bottom tubes in the domain also consist of a wake with one vortex forming its recirculation region. Considering the symmetry of the modeled tube bundle arrangement, top and bottom's tube vortex model one half of the wake region of the center tube displayed in Fig. 5.

4.2.2 Local Flow Field Analysis

Fig. 6a and 6b show local distributions of velocity, static pressure and temperature normal to flow direction for selected flow passages in the flow domain. Fig. 6a presents local parameter distributions upstream of the selected flow passage and Fig. 6a presents local parameter distributions downstream of the selected flow passages.
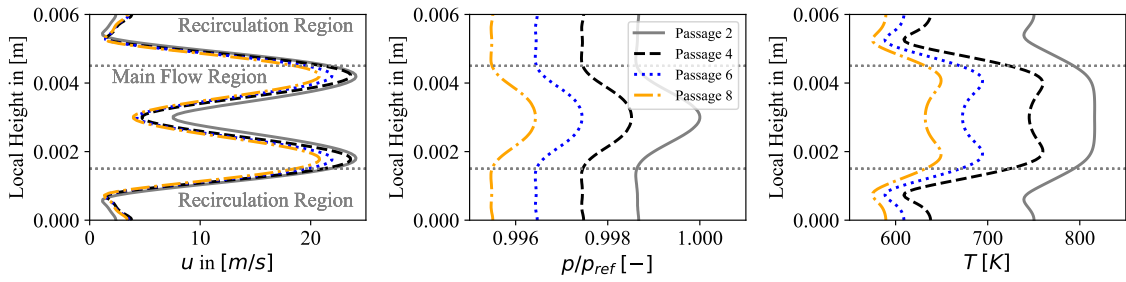
(a) Local parameter distribution upstream of the selected flow passages. The reference pressure p_{ref} is the maximum pressure of the upstream rake of the second flow passage
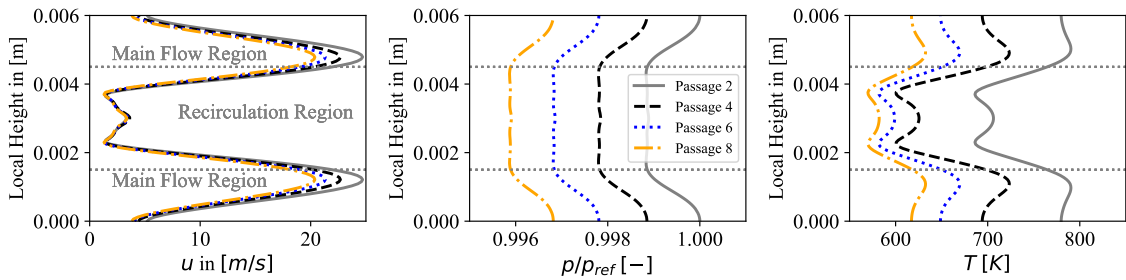
(b) Local parameter distribution downstream of the selected flow passages. The reference pressure p_{ref} is the maximum pressure of the downstream rake of the second flow passage

8

The local static pressure distribution for both plots reveals several constant pressure regions marked by dashed lines in the presented figure. These regions indicate the recirculation region along the respective rake. In Fig. 6a these values are located at the top and bottom boundary of the domain due to the fact that the usptream rake of the selected flow passage faces the wake of the contours at top and bottom boundary. The local recirculation region in Fig. 6b is located at the center of the domain caused by the wake of the center contour in that selected flow passage.

Within these constant pressure regions, velocity and temperature levels are dropped reaching minimal value. As the rake is located in the middle between both neighbouring flow passages, the rake does not exactly meet the center of the wake vortices, but an x-position close to the vortex center. This explains the local velocity minima not reaching a value of 0 m/s in the presented plots. It is recognizable that the main decrease in velocity magnitude and temperature takes place inside the recirculation region.

The region outside of the recirculation region represents the X-type main flow through the tube bundle. Outside of the constant pressure region at certain heights in the plots, local pressure, velocity and temperature maxima are visible. The local pressure maxima are a result of the rake in that height being close to the stagnation point region of either the center tube or the top and bottom tubes. Getting closer to the stagnation point in turn also means a lower velocity level of the flow. The peak value of the local pressure distribution decreases with increasing passage number as the velocity magnitude also decreases along its path through the domain. Therefore, the pressure increase due to the reduction of the dynamic pressure is decreased. Therefore both, the static pressure and the dynamic part of the total pressure decrease along the flow path in the domain. The local velocity and temperature peaks in the main flow region outside the recirculation region are a result of the local acceleration of the flow around the contour's surface. The velocity and temperature peak values are decreased with increased passage number as the local velocity level is also decreased along its flow path through the domain. In the second flow passage the local velocity magnitude has its maximum value leading to an enhanced increase in dynamic temperature for the rakes upstream the second flow passage.

4.3   The Local Heat Transfer Coefficient

Fig. 7 presents the local heat transfer coefficient along the perimeter of the tube based on the computed local wall heat flux distribution from the stagnation point at $\varphi = 0°$ until $\varphi = 180°$. On the left hand side, the local heat transfer coefficient of the first five passages and on the right hand side the local heat transfer coefficient of the last five passages of the CFD domain are plotted.

The curves in both plots show that the local heat transfer coefficient at $\varphi = 180°$ compared to the stagnation point value is decreased as the local heat transfer coefficient depends on the development of the thermal boundary layer thickness. At the stagnation point, the thermal boundary layer thickness has its smallest value. Therefore, the temperature gradient at the tube wall has its highest value leading to a high heat transfer coefficient in the stagnation point. As the velocity boundary layer thickness increases along the tube's contour, the thermal boundary layer also increases its thickness and thus decreases the local heat transfer coefficient.
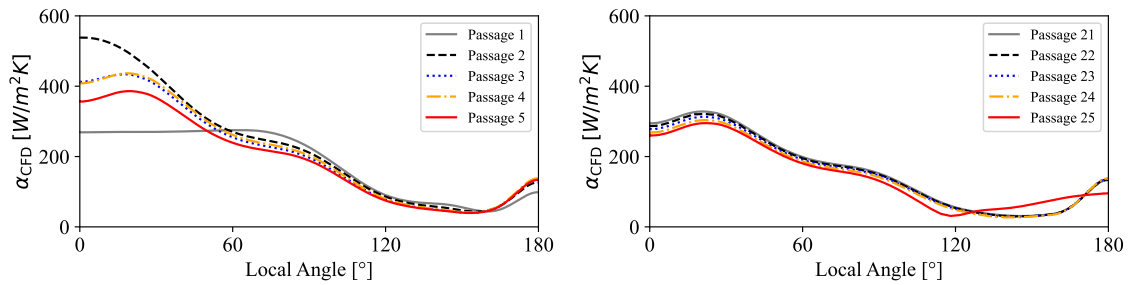
Figure 7: The local heat transfer coefficient along the perimeter of the tube for the first five flow passages (left) and the last five flow passages (right)

The local heat transfer coefficient in the first five flow passages reveals that the local distribution

of the heat transfer coefficient in the first flow passage differs from the remaining curves. Unlike the inside flow passages, the first flow passage faces a uniform and non-perturbated inlet flow, especially influencing the heat transfer characteristics in the front part of the tube in the first flow passage. The top and bottom tube rows of the first flow passage reduce the cross sectional area significantly causing a nozzle-like acceleration of the flow. The second passage, therefore, faces much higher velocity levels and higher local Reynolds numbers than the first flow passage. The higher Reynolds numbers lead to higher Nusselt number and with moderate temperature change over the first flow passage to much higher heat transfer coefficients in the second flow passage.

Downstream of the second flow passage the characteristics of the distribution of the heat transfer coefficient does not change qualitatevily. This suggests that the flow is fully developed starting from the third passage and no *inlet flow effects* are visible anymore. All tubes located in the inner part of the tube bundle arrangement show local peaks in the heat transfer coefficient distribution caused by local velocity maxima due to the change in local cross sectional area. The cool down of the flow leads to a shift of the local heat transfer distributions towards lower values. The last flow passage, however, shows slight deviations compared to its upstream flow passages. As the exhaust flow exits the tube bundle, *outflow effects* in terms of a high velocity jet and an enlarged recirculation region of the last tube, increase the local heat transfer coefficient in the rear part of the last tube.

4.4 Thermal Analysis

In order to evaluate the thermal behaviour of the modeled heat exchanger setup, area weighted averages of the local heat transfer coefficient and the local Nusselt number for each tube in the domain are computed. Fig. 8 presents a Nusselt number distribution as well as a distribution of computed heat transfer coefficients along the flow passages of the tube bundle arrangement compared to the correlation-based prediction of these values.
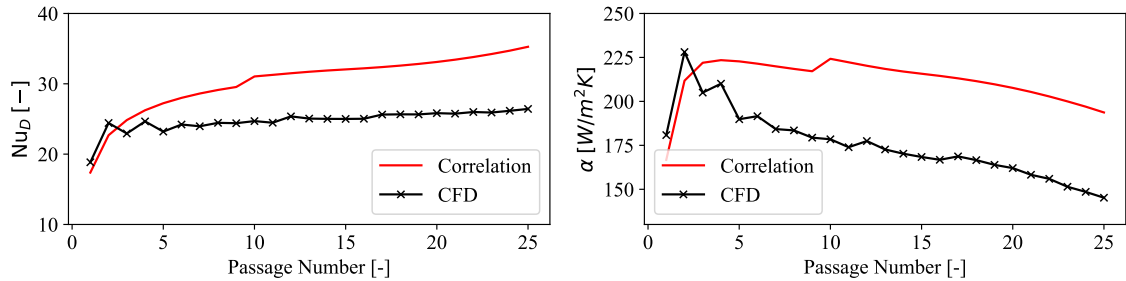
Figure 8: Development of the Nusselt number and heat transfer coefficient along the flow passage in the domain

It is shown that with increasing passage number the Nusselt number Nu_D computed based on the CFD results increases along the flow path of the fluid. There is a strong increase from first to second flow passage due to the turbulence development inside the tube bundle. After the second passage, however, there are no major steps noticeable, but there is still a slight increase in Nusselt number. The correlation-based prediction depicts the same trend of the development of Nusselt number and heat transfer coefficient, but qualitatively overpredicts the Nusselt number in the repsective flow passage.

The average contour's heat transfer coefficient, however, decreases with increasing passage number, but has a global maximum at the second passage. A minimal thermal resistance or maximum heat transfer coefficient in the second flow passage has been observed in recent publications as well, see [8]. As the exhaust flow is cooled down along its path through the tube bundle, the thermal conductivity is also decreased throughout the domain. The thermal conductivity decreases stronger than the Nusselt number increases leading to a decreasing heat transfer coefficient through the domain. Both, the CFD results as well as the correlation-based prediction depict this trend. The correlation, however, does not show a local maximum on the second flow passage.

As mentioned in the previous section, there are *inlet flow effects* influencing the thermal behaviour of the exhaust flow in the first passages. The strong increase in the Nusselt number and heat transfer coefficient from first to second passage represents these effect. In the averaged results of Nusselt number and heat transfer coefficient the *outflow effects* are not visible anymore. The outflow effects also seem to not influence the thermal behaviour of upstream tubes.

A decreasing heat transfer coefficient means in turn that the thermal resistance of the exhaust flow throughout the domain is increased. As the thermal resistance of the exhaust side builds up the dominating part of the overall thermal resistance in the HRSG, the development of the heat transfer coefficient is of major importance for the design of the HRSG.

4.5   Hydraulic Analysis

The hydraulic behaviour of the tube bundle is investigated using the Reynolds number following Eq. (3) and the total pressure loss over the flow passages. The passage pressure loss is determined by computing an area weighted average of the total pressure distribution over a vertical rake and computing the delta from upstream to downstream rake.

Fig. 9 presents trends for the local Reynolds number, the velocity magnitude of the flow and the passage total pressure loss over the flow passages. The plotted passage Reynolds number is a result of PreHEAT computations. Therefore, the velocity magnitude computed by PreHEAT relevant for the Reynolds number computation is used to indicate that the velocity level decreases and the local Reynolds number increases throughout the domain. The local Reynolds number obviously varies from values of
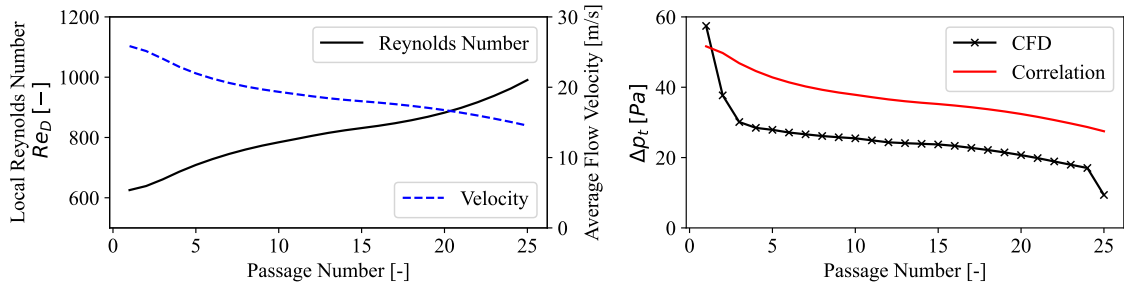
Figure 9: Development of local Reynolds number and passage pressure loss over the flow passages in the domain

above $Re \approx 600$ to values of about $Re \approx 1000$ meaning that the ratio of inertia forces to viscous forces of the flow is enhanced through the domain. Due to the cool down of the flow, the viscosity decreases and compensates the decreased velocity level along the flow path, so that in total the Reynolds number increases its values. A non-linear increase in Reynolds number is caused by a non-linear change of temperature over the flow passages leading also to a non-linear change in velocity magnitude.

The passage total pressure loss decreases over the flow passages with a non-linear behaviour. There is maximum pressure loss of nearly $\Delta p_t \approx 60$ Pa over the first flow passage and a decrease to below $\Delta p_t \approx 10$ Pa over the last flow passage. The decrease in total pressure loss over the passages is caused by a decreased velocity level through the domain. The strong reduction of pressure loss in the first flow passages is caused by *inlet flow effects* causing a strong turbulence production of the flow entering the tube bundle. After the exhaust flow is fully developed inside the tube bundle, the pressure loss decreases nearly linearly until the last flow passage. *Outflow effects* cause the passage pressure loss of the last passage to drop non-linearly to other values.

The correlation-based prediction of the passage pressure loss on global scale depicts a similar trend compared to the CFD results. The *inflow and outflow effects* for the passage pressure loss are not depicted as clearly as the CFD computation does. However, there is a slight non-linearity recognizable for the first and last flow passages.

4.6 Rake Position Dependency

As mentioned previously, several vertical rakes are positioned inside the CFD domain to monitor the passage thermal and hydraulic behaviour. The vertical rakes inside the tube bundle are always positioned in the center of the gap between neighbouring tubes. Inlet and outlet rake, however, upstream of the first flow passage and downstream of the last flow passage have to be positioned as well. A general assumption of an ideal position for the inlet and outlet rake has been made with a dimensionless distance of $f/d = 6.0$. This study varies the position of the inlet and outlet rake to evaluate their effect on the total pressure loss evaluation over the flow passages. Therefore, Fig. 10 presents the passage pressure loss behaviour with varying x-positions of the inlet and outlet rake. The dimensionless distance of the inlet and outlet rake to the tube bundle is kept equal. Therefore, an equal dimensionless distance is computed to:

$$\frac{f}{d} = \left(\frac{f}{d}\right)_{in} = \left(\frac{f}{d}\right)_{out}. \tag{6}$$

In the center of Fig. 10, the global behaviour of the passage pressure loss is shown. On the left hand side, the pressure loss behaviour of the first three passages is plotted. On the right hand side, however, it is zoomed into the passage pressure loss behaviour of the last three flow passages.
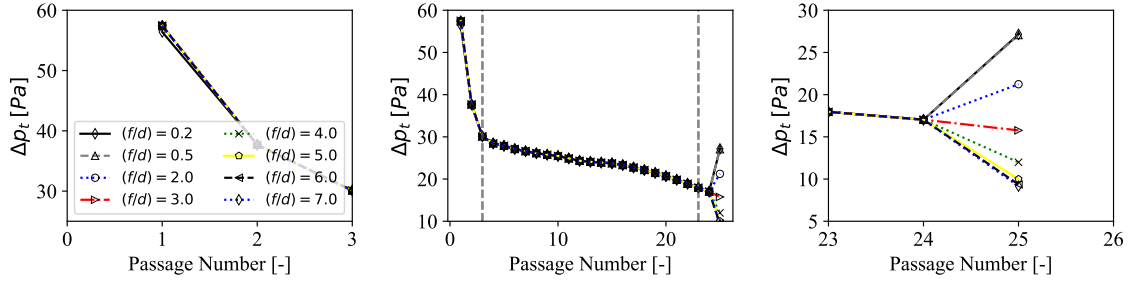
Figure 10: Effect of varying x-position of the inlet and outlet rake on the pressure loss behaviour

It is recognizable that with increasing distance to the tube bundle, the inlet passage pressure loss does not vary as much as the outlet passage pressure loss does. The inlet total pressure loss is nearly constant with $\Delta p_t \approx 55-57$ Pa. The outlet total pressure loss varies within $\Delta p_t \approx 10-30$ Pa. An outlet rake positioned close to the last tube row covers a range of its vertical length inside the recirculation region of the last tube row and a part of its height in the high velocity outflow jet of the tube bundle, see Fig. 11. In Fig. 11, recirculation regions are recognizable by negative values of the horizontal velocity component u_x.

In total, there is a combination of three effects causing the averaged rake's total outlet pressure to increase with higher f/d values. First, in the wake of a tube, the total pressure is always lower than in the main flow region, visible in Fig. 11 on the right hand side. Increasing the distance from the last tube row means an increase in static pressure due to being outside of the wake. Second, close the last tube row, the rake is also located within the high velocity jet causing an increase in total pressure due to a higher velocity level in this region. This high velocity jet, however, reduces its velocity magnitude towards the outlet boundary causing the total pressure increase to flatten out with increased f/d value. Third, in the present case, the static pressure downstream the last tube row is also lower than the defined static pressure at the outlet of the CFD domain causing the static pressure to increase towards the outlet boundary. Therefore, increasing the f/d value means to distance the rake from the constant pressure recirculation region and the high velocity outflow jet and at the same time increasing the static pressure due to being closer to the outlet boundary.

It is shown that for values equal or above $f/d = 4.0$, the outlet rake is positioned, so that no part of its vertical range is covered in the recirculation region and the impact due to the high velocity jet is also decreased, see Fig. 11. For values greater than $f/d = 4.0$, the high velocity jet impact is further reduced and no major changes in the local velocity and total pressure curves are noticeable, especially for $f/d = 6.0$ and $f/d = 7.0$.
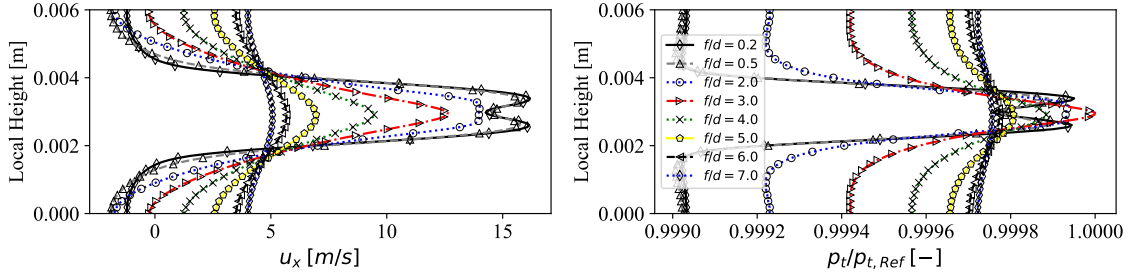
Figure 11: Effect of varying x-position of the outlet rake on the local horizontal velocity component and on the local total pressure distribution. The reference total pressure $p_{t,Ref}$ is the maximum total pressure for $f/d = 3.0$

The variation of the rake's x-position in the presented study reveals that the recirculation region is no longer present for a dimensionless position of greater than $f/d = 4.0$. As no changes in the outlet passage pressure loss are noticeable for values of $f/d \geq 6.0$, a value of $f/d = 6.0$ is chosen as default value for the rake's x-positions.

As the reference temperature for the computation of the heat transfer coefficient is computed based on the energy balance, the changes in the outside pressure with varying x-position can have an effect on the reference temperature and the heat transfer coefficient. Preliminary studies, however, showed that the change in pressure due to the rake's outlet position has a negligible effect on the *energy balance based reference temperature* and thus there are no changes in the heat transfer coefficient for the last and first tube row with varying x-position of the rake.

5   Conclusion and Outlook

In summary, the current publication presents CFD results for a possible setup of the HRSG of the WET concept. An implemented coupled approach between a preliminary design tool and 2D steady CFD analysis is applied to generate the presented CFD results. The focus of this publication is on the analysis of the computed local and global thermal and hydraulic behaviour of the modeled heat exchanger setup.

The heat exchanger flow type is defined as a cross counter flow configuration with steam loaded exhaust gas as hot fluid and water on the inside of the tubes as cold fluid side. The setup of the HRSG is formed by a defined staggered arrangement of parallel tubes with a specific number of flow passages. The flow field of the modeled HRSG setup is assumed to be steady. Turbulence modeling using the $k\omega$-SST model considers the turbulent nature of the flow inside the tube bundle arrangement. The CFD results on global scale depict the expected cool down of the flow along its flow path through the domain influencing the velocity level of the exhaust flow through the domain. The changing velocity level has an influence on both, the thermal and hydraulic behaviour of the flow. The heat transfer coefficient decreases along the flow passages as well as the pressure losses. Varying the local vertical rake's x-position placed downstream of the last tube row influences the outlet total pressure loss of the tube bundle significantly.

In future, several turbulence modeling approaches have to be considered to evaluate their effect on the qualitative thermal and hydraulic behaviour of the HRSG. The consideration of fins in the CFD model would enhance the modeling capability of the CFD analysis and thus widen the design space for the implemented coupled approach between PreHEAT and CFD. Based on the implemented coupled approach, several operating conditions for one design will be computed, so that numerical correlations for the exhaust side heat transfer and pressure loss behaviour of the HRSG can be derived. In a next step, these numerical correlations need to be validated with experimental data.

Acknowledgements

Supported by:

Federal Ministry
for Economic Affairs
and Climate Action

on the basis of a decision
by the German Bundestag

References

[1] Sascha Kaiser, Oliver Schmitz, Paul Ziegler, and Hermann Klingels. The water-enhanced turbofan as enabler for climate-neutral aviation. *Applied Sciences (MDPI)*, 12, 2022.

[2] Oliver Schmitz, Herrmann Klingels, and Petra Kufner. Aero engine concepts beyond 2030: Part 1 – the steam injecting and recovering aero engine. 143(2), 2021.

[3] Alexander Görtz, Jannik Häßy, Marc Schmelcher, and Mahmoud El-Soueidan. Water enhanced turbofan: Improved thermodynamic cycle using hydrogen as fuel. *Proceedings of the ASME Turbo Expo 2023*, 2023.

[4] Paul Ziegler, Sascha Kaiser, and Volker Gümmer. Parametric cycle studies of the water-enhanced turbofan concept. *ASME Turbo Expo 2023: Turbomachinery Technical Conference and Exposition*, 2023.

[5] Marc Schmelcher, Jannik Häßy, Alexander Görtz, and Mahmoud El-Soueidan. Methods for the preliminary design of heat exchangers in aircraft engines. *Proceedings of the ASME Turbo Expo 2023*, 2023.

[6] D. Missirlis, K. Yakinthos, A. Palikaras, K. Katheder, and A. Goulas. Experimental and numerical investigation of the flow field through a heat exchanger for aero-engine applications. *International Journal of Heat and Fluid Flow*, 26:440–458, 2005.

[7] D. Missirlis, S. Donnerhack, O. Seite, C. Albanakis, A. Sideridis, K. Yakinthos, and A. Goulas. Numerical development of a heat transfer and pressure drop porosity model for a heat exchanger for aero engine applications. *Applied Thermal Engineering*, 2010.

[8] D. Missirlis, M. Flouros, and K. Yakinthos. Heat transfer and flow field investigation of heat exchanger for aero engine applications. *International Journal of Heat and Technology*, 29(2):54–64, 2011.

[9] D. Missirlis, Z. Vlhaostergios, M. Flouros, C. Salpingidou, S. Donnerhack, A. Goulas, and K. Yakinthos. Optimization of heat exchangers for intercooled recuperated aero engines. *MDPI Aerospace*, 2017.

[10] Kyros. J. Yakinthos, Dimitris K. Missirlis, Achilles C. Palikaras, and Apostolos K. Goulas. Heat exchangers for aero engine applications. (IMECE2006-13667), 2006.

[11] Z. Vlahostergios, D. Misirlis, M. Flouros, S. Donnerhack, and K. Yakinthos. Efforts to improve aero engine performance through the optimal design of heat recuperation systems targeting fuel consumption and pollutant emissions reduction. *12th European Conference on Turbomachinery Fluid Dynamics and Thermodynamics*, 2017.

[12] Mahmoud El-Soueidan, Marc Schmelcher, Jannik Häßy, and Alexander Görtz. The coupling of a preliminary design method with cfd analysis for the design of heat exchangers in aviation. *AIAA Aviation*, 2024.

[13] Mahmoud El-Soueidan, Marc Schmelcher, Alexander Görtz, Jannik Häßy, and Marius Bröcker. Integration of a gas model into computational fluid dynamics analysis for the simulation of turbine exhaust flows with high steam loads. *ASME Journal of Engineering for Gas Turbines and Power*, 2023.

[14] Peter Stephan, Stephan Kabelac, Matthias Kind, Dieter Mewes, Karlheinz Schaber, and Thomas Wetzel. *VDI-Wärmeatlas.* Springer Berlin Heidelberg, Berlin, Heidelberg, 2019.

[15] John R. Thome. *Encyclopedia of two-phase heat transfer and flow I: Fundamentals and methods.* World Scientific, New Jersey, 2015.

[16] S. Umeda and W.-J. Yang. Interaction of von karman vortices and intersecting main streams in staggered tube bundles. *Experiments in Fluids*, 26:389–396, 1999.